RESEARCH ARTICLE | APRIL 16 2026

Fluctuation-induced dynamo electromotive forces in current-driven tokamak sawtooth relaxation

K. J. McCollam ; B. E. Chapman ; J. S. Sarff ; R. A. Myers ; M. D. Pandya ; R. Xie

Phys. Plasmas 33, 042507 (2026)
https://doi.org/10.1063/5.0300072

Physics of Plasmas ARTICLE pubs.aip.org/aip/pop

Fluctuation-induced dynamo electromotive forces in current-driven tokamak sawtooth relaxation

Cite as: Phys. Plasmas **33**, 042507 (2026); doi: 10.1063/5.0300072
Submitted: 30 August 2025 · Accepted: 17 March 2026 ·
Published Online: 16 April 2026

K. J. McCollam,[a] B. E. Chapman, J. S. Sarff, R. A. Myers, M. D. Pandya, and R. Xie

AFFILIATIONS

Department of Physics, University of Wisconsin–Madison, Madison, Wisconsin 53706, USA

[a]Author to whom correspondence should be addressed: kmccollam@wisc.edu

ABSTRACT

We show how a fluctuation-induced dynamo electromotive force (EMF) is responsible for a Kadomtsev-like, current-driven tokamak sawtooth cycle in zero-thermal-pressure, visco-resistive magnetohydrodynamics (MHD), via nonlinear simulations performed with the NIMROD code. We observe a pulsing fluctuation-induced dynamo EMF that, synchronous with time-evolving fluid velocity and magnetic fluctuation energies, arises naturally in the relaxation process, repeatedly driving the safety factor q profile within the $q = 1$ surface from below to above unity during the quasiperiodic crash-like relaxation events, each with a change in on-axis q of roughly $\Delta q_0 \approx 0.1$. We show how the structures of the velocity and magnetic fluctuations lead to the form of the dynamo EMF and how its structure changes during the sawtooth cycle, consistent with its current profile flattening effect in the sawtooth crash. The process demonstrates the importance of the inductive plasma response in balancing the dynamo in sawtooth activity. We also discuss higher-dissipation cases exhibiting steady helical cores, whose quiescent dynamo EMF modifies the equilibrium profile in a way similar to sawtooth crash relaxation. This work expands the description of the MHD dynamo's importance beyond its role in maintaining quiescent core q profiles in sawtoothing or sawtooth-free tokamak states to its role in modulating the q profile during current-driven sawtooth activity.

I. INTRODUCTION

Tokamak sawtooth activity[1,2] is an often observed feature of modern experiments[3–5] and is expected to affect planned burning plasma operations.[6,7] Sawtooth oscillations are named for the characteristic shape of temporal waveforms of the quasiperiodic crashes in measured core temperature typically activated when q_0, the on-axis value of the safety factor q, which is the ratio of toroidal to poloidal transits for magnetic field lines, is sustained at or below unity. Sawteeth have significant fusion performance-related effects,[8–14] motivating the development of methods of sawtooth control[15–18] as well as sawtooth avoidance via operation in advanced tokamak scenarios[19] with $q_0 > 1$, including the hybrid scenario.[20–23] For present and future operations relating to sawteeth, predictive capability via a more comprehensive understanding of their properties and dynamics is an important overarching goal.

In the early and influential Kadomtsev conceptual model of the sawtooth mechanism,[24] as q_0 is driven below unity by current drive, a kink mode with poloidal m and toroidal n mode numbers $(m, n) = (1, 1)$ resonates at the $q = m/n = 1$ magnetic surface, creating a magnetic island and instigating a sawtooth crash as a Sweet-Parker resistive reconnection event. The island magnetic flux replaces the previous toroidally symmetric core, accompanied by magnetic stochasticity and rapid outward thermal transport, as $q_0 > 1$ is restored, and the cycle repeats. A number of other conceptual models have been developed[25–28] to address the gaps between the Kadomtsev model and a variety of experimental observations,[2,29–31] and the validation of sawtooth modeling in experiment remains an active topic.[32–35] Sawtooth activity has been investigated using numerical modeling of nonlinear magnetohydrodynamics (MHD) from various perspectives.[28,29,32,33,35–50]

One phenomenon of fundamental importance in the context of both sawtoothing and hybrid tokamak plasmas is the fluctuation-induced MHD "dynamo" electromotive force (EMF),[51] previously investigated in the context of magnetic relaxation and equilibrium sustainment in reversed-field pinches (RFPs),[51–57] spheromaks,[58–60] and spherical tokamaks,[61–63] and edge-localized modes[64] and vertical displacement events[65] in tokamaks. This quantity is the nonlinear correlation $\langle (\tilde{\boldsymbol{V}} \times \tilde{\boldsymbol{B}})_\parallel \rangle$ between fluid velocity $\tilde{\boldsymbol{V}}$ and magnetic field $\tilde{\boldsymbol{B}}$ fluctuations in the parallel mean-field single-fluid resistive MHD Ohm's law,

$$\langle E_\parallel \rangle + \langle (\tilde{\boldsymbol{V}} \times \tilde{\boldsymbol{B}})_\parallel \rangle = \langle \eta J_\parallel \rangle, \tag{1}$$

which exposes its possible current- or anti-current drive effects; here, $\boldsymbol{E}$ is the electric field, η is the plasma resistivity, and $\boldsymbol{J}$ is the current density.

The dynamo effect is thought to be responsible for the experimentally observed process in tokamaks called "flux pumping."[21,35,57,66–68] In the flux-pumping hypothesis of Jardin *et al.*[69,70] for a hybrid-like scenario in finite-thermal-pressure MHD, a saturated $(1, 1)$ interchange mode provides a steady anti-current dynamo EMF maintaining q_0 steadily just above unity, preventing sawtooth activity. A similar dynamo model also accounts for sawtooth activity with a quiescent q profile.[28] Other recent finite-thermal-pressure MHD tokamak simulations show dynamo effects to be fundamental to the development and maintenance of sawtooth-free states.[33,35] Recent experiments on DIII-D[71] have demonstrated the need for a fluctuation-induced EMF to explain core electric field measurements during tokamak sawtooth activity.[72]

In this paper, we show that a dynamo EMF due to resistive internal kink-like mode activity is active throughout current-driven, Kadomtsev-style[24] tokamak sawteeth in visco-resistive, single-fluid, zero-thermal-pressure MHD, via nonlinear simulations in toroidal geometry using the NIMROD code.[73] Thus, we have intended to use a relatively simple MHD model that produces sawteeth. We observe a pulsing dynamo EMF that, synchronous with time-evolving velocity and magnetic fluctuation energies, arises naturally in the relaxation process, repeatedly driving the core q profile from below to above unity during the crash-like relaxation events in a quasiperiodic sawtooth cycle. In our simulations, the change in q_0 at the sawtooth crash is roughly $\Delta q_0 \approx 0.1$. We show how the structures of the velocity and magnetic field fluctuations lead to the dynamo EMF as well as how its radial structure changes during the sawtooth cycle, in particular, the crash phase. The dynamo EMF extends spatially from the magnetic axis to just outside the $q = 1$ surface, where its sense changes from anti-current drive inside to current drive outside, consistent with local flattening of an initially peaked current profile. We show the fundamental importance of the interaction between dynamo EMF and plasma inductive response in driving the tokamak sawtooth dynamics. We also perform simulations with higher dissipation parameters to produce steady helical cores whose dynamo EMF has a similar effect on the toroidally symmetric tokamak profiles to that of the crash in the sawtoothing cases, demonstrating the foundational character of the dynamo effect. Beyond the dynamo's role in maintaining a relatively quiescent core q profile in sawtoothing or sawtooth-free states, the focus of previous related works using finite-thermal-pressure MHD,[28,33,35,69,70] this work emphasizes that the dynamo has a continuous modulating effect on the q profile in the current-driven sawtooth regime in zero-thermal-pressure MHD.

This paper is organized as follows. Section II describes how the simulations are set up; the key results are described for sawtoothing cases in Sec. III A and for steady-state cases in Sec. III B, and these are discussed in Sec. IV.

II. SIMULATIONS

Our NIMROD[73] simulations implement a zero-thermal-pressure, incompressible, visco-resistive single-fluid MHD model in toroidal geometry, including a momentum equation $\rho \mathrm{d}\boldsymbol{V}/\mathrm{d}t = \boldsymbol{J} \times \boldsymbol{B} + \rho \nabla \cdot \nu \nabla \boldsymbol{V}$ and an Ohm's law $\boldsymbol{E} + \boldsymbol{V} \times \boldsymbol{B} = \eta \boldsymbol{J}$, where $\boldsymbol{V}$ is the fluid velocity, $\boldsymbol{J}$ is the current density, $\boldsymbol{B}$ is the magnetic field, $\boldsymbol{E}$ is the electric field, and ρ, ν, and η are static scalars representing the uniform mass density, the kinematic viscosity, and the electrical resistivity, respectively. NIMROD uses Faraday's law to evolve $\boldsymbol{B}$ and Ampère's law to calculate $\boldsymbol{J}$. Further details on the NIMROD algorithm are available in Ref. 73, including the boundary conditions on $\boldsymbol{E}$, $\boldsymbol{V}$, and $\boldsymbol{B}$. In terms of the computation domain, the simulated tokamak plasmas have aspect ratio $R_0/a = 3$, where R_0 is the major radius of the geometric magnetic axis and a is the midplane minor radius and elliptical cross sections with vertical elongation $\kappa = 1.8$. The value of Lundquist number $S \equiv \tau_{\mathrm{res}}/\tau_{\mathrm{A}}$ at the magnetic axis is set approximately to $S_0 \approx 10^5$, where $\tau_{\mathrm{res}} \equiv \mu_0 a^2/\eta_0$ is the resistive diffusion time using the on-axis resistivity η_0, $\tau_{\mathrm{A}} \equiv a\sqrt{\mu_0 m_{\mathrm{i}} n_{\mathrm{d}}}/B_0$ is the core Alfvén time, μ_0 is the vacuum magnetic permeability, m_{i} is the ion mass, n_{d} is the plasma density, and B_0 is the toroidally symmetric $n = 0$ part of the magnetic field strength at the magnetic axis. The magnetic Prandtl number $P_{\mathrm{m}} \equiv \tau_{\mathrm{res}}/\tau_{\mathrm{visc}} = \mu_0 \nu/\eta$ is set to $P_{\mathrm{m}} = 1$ everywhere in the plasma, where $\tau_{\mathrm{visc}} \equiv a^2/\nu$ is the viscous diffusion time. Time values in the simulations are normalized approximately to the Alfvén time by setting a, μ_0, m_{i}, and n_{d} equal to 1 and arranging for B_0 to be approximately equal to 1, such that $\tau_{\mathrm{A}} \approx 1$. Spatial resolution of the poloidal plane is provided by an 80×80 polar grid of 4×4 (biquartic) finite elements. The toroidal direction is spectrally resolved by toroidal mode numbers n of 0 through 10.

Thus, an n spectrum is inherent in the output field data for each poloidal grid location, while a poloidal mode number m spectrum for an output field quantity would need to be calculated post hoc, which we have not done in this work. Note that in the analysis described later, we use curly brackets as in "$\{x\}$" for the toroidal average of a field quantity x, defined at each poloidal point, and then its flux-surface average $\langle x \rangle$, written with angle brackets, is the average of $\{x\}$ around a poloidal flux surface.

We use two sawtoothing simulation cases in which the tokamak equilibria are numerically set up and sustained in different ways to investigate how this might affect sawtooth evolution dynamics. As a result, we find that both cases show very similar dynamo EMF behavior in the sawtooth cycle. Each case has a peaked current profile and

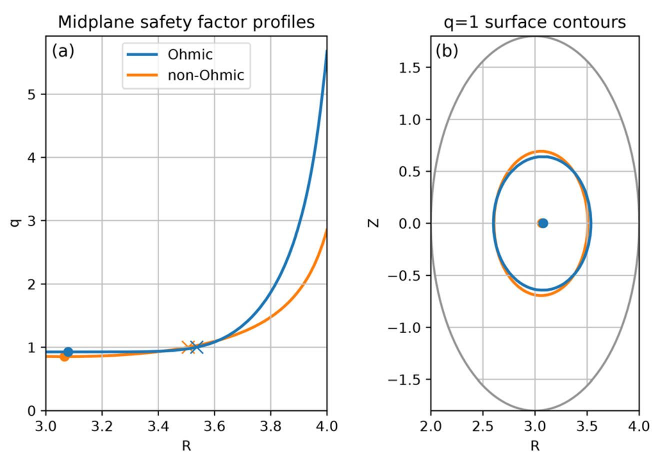

FIG. 1. Initial ($t = 0$) equilibrium q structure for the Ohmic and non-Ohmic sawtoothing cases in blue and orange, respectively. (a) q vs (outboard) major radius R, with respective $q = 1$ locations marked with diagonal crosses. (b) $q = 1$ surfaces in the poloidal plane vs major radius R and vertical position Z, with fixed plasma boundary in gray. In both plots, dots indicate the respective magnetic axes.

hollow q profile with outboard midplane $q = 1$ radius of $\sim a/2$, as summarized in Fig. 1.

One sawtoothing case, labeled as "Ohmic," is motivated by an experimental scenario in which a certain plasma current is targeted with variable, feedback-controlled Ohmic loop voltage $V_{\rm loop}$. The plasma is initialized with a background toroidal magnetic field, zero plasma current, and a spatially fixed hollow η profile, to which $V_{\rm loop}$ is applied. The η profile is given by $\eta_0[1 + (\sqrt{\texttt{dvac}} - 1)\rho^{\texttt{dexp}}]^2$, where ρ is the boundary-normalized logical radial variable, the boundary value is dvac $= 400$, and the exponent is dexp $= 6$. At first, only $n = 0$ dynamical evolution is enabled in the NIMROD time advance, and the plasma evolves via loop voltage feedback to a steady state with the preset target current and $q_0 = 0.93$, after which point $n > 0$ fluctuations are also enabled at a nominal time of $t = 0$, and nonlinear evolution proceeds.

The other sawtoothing case, labeled as "non-Ohmic," is based on another way to set up the NIMROD time advance reminiscent of an experimental scenario that includes non-inductive current drive. The plasma is initialized with a preset Grad–Shafranov equilibrium with $q_0 = 0.85$ using the NIMEQ equilibrium solver[74] with a Grad–Shafranov $F(\psi_{\rm norm})$ profile $\texttt{f\_open} + \texttt{f1\_closed}(1 - \psi_{\rm norm}) + 4 \times \texttt{f2\_closed} \times \psi_{\rm norm}(\psi_{\rm norm} - 1)$, where $\psi_{\rm norm}$ is the normalized poloidal flux, $\texttt{f\_open} = 3.0$, $\texttt{f1\_closed} = 0.285$, and $\texttt{f2\_closed} = 0.07125$. In this case, there is no explicit loop voltage applied, and the resistivity is uniform at the value η_0. Starting at $t = 0$, NIMROD advances the nonlinear time evolution of $n \geq 0$ perturbations from this steady state, such that the instantaneous $n = 0$ component is the sum of the initial equilibrium, which is not time-advanced, and the time-varying $n = 0$ component. We note that this simulation workflow is simpler than for the Ohmic case, in that here, there is no need to first evolve an equilibrium using the time advance.

Thus, the key difference between the two sawtoothing cases is that in the Ohmic case, loop voltage induction of the bulk current profile is included in the time advance, and in the non-Ohmic case, it is not. The input energy is explicit in the Ohmic case and implicit in the non-Ohmic case, but in both cases, fluctuations and nonlinear interactions between them drive the dynamics, and the resulting dynamics, including the fluctuation-induced EMF, are very similar, as we will show later.

The $t = 0$ equilibrium radial q profiles for both cases are shown in Fig. 1(a), and the $q = 1$ magnetic flux surfaces in the poloidal plane are shown in Fig. 1(b), with the fixed plasma boundary indicated in gray. Note in Fig. 1(b) that the $q = 1$ surface is slightly more oblate for the Ohmic case than for the non-Ohmic case.

In order to compare with the main characteristics of the dynamo EMF in the sawtoothing cases, we also perform another set of simulations with plasma dissipation increased sufficiently for the tokamak to reach a steady state, with a helically distorted core which generates a quiescent dynamo EMF. This program has been carried out previously in MHD simulations of RFP[46,54,55,75] and tokamak[45,46] plasmas, and the resulting state is reminiscent of other quiescent helical states in finite-thermal-pressure MHD tokamak simulations[33,35,69] and in experiments,[57] though as it originates here simply from an *ad hoc* increase in scalar dissipation, it does not necessarily correspond closely with them physically.

The increased-dissipation case which we present has the same initial equilibrium, spatially flat resistivity η, and $S = 10^5$ value as the non-Ohmic sawtoothing case discussed earlier, while the kinematic viscosity ν is increased to make $P_{\rm m} = \mu_0\nu/\eta = 10^3$, so that the Hartmann number $H \equiv \sqrt{\tau_{\rm res}\tau_{\rm visc}}/\tau_{\rm A} = S/\sqrt{P_{\rm m}}$, which is the determinative MHD dissipation parameter for negligible inertia,[75] is $H \approx 3 \times 10^3$, compared to $H = 10^5$ for the sawtoothing cases.

III. RESULTS

A. Sawtoothing

Both of the sawtooth simulation cases exhibit nonlinear oscillation behavior corresponding to Kadomtsev sawteeth, as shown in the form of magnetic fluctuation energies vs time in Fig. 2. After initial stages of linear mode growth and nonlinear settling, the $n = 1$ magnetic energies are dominant for most of the regular sawtooth cycles in each case, though in the non-Ohmic case, the $n = 2$ briefly becomes as large as the $n = 1$ around the time of the crash (rapid decrease) in $n = 1$ amplitude. The observed spread in fluctuation energies from $n = 1$ to 10 is at least a few orders of magnitude at all times during the regular sawtooth cycles, indicating that these simulations have sufficient toroidal resolution.[41] For each case in Fig. 2, the black vertical line near the respective sawtooth crash time for $n = 1$ energy during a single sawtooth cycle ($t = 16\,264.959$ and $t = 16\,735.391$, respectively) indicates the time chosen for a single-time Ohm's law balance analysis, described later, at which the dynamo EMF is approximately at its maximum amplitude for the sawtooth cycle. The shaded time window in Fig. 2(b) ($14\,865 \leq t \leq 18\,745$) will also be examined later on.

The spatial structures of the constituent fields generating the dynamo EMF in the non-Ohmic sawtoothing case are shown in Fig. 3 for the single-time point indicated in Fig. 2(b). The corresponding results for the Ohmic case are similar, not shown here for brevity. Characteristic of a resistive internal kink-like mode, these fields are mainly located near and within the $q = 1$ surface. The velocity fluctuation $\tilde{\boldsymbol{V}}$ in Figs. 3(a) and 3(b) has a large vortical, interchange-like structure, while the magnetic fluctuation $\tilde{\boldsymbol{B}}$ in Figs. 3(c) and 3(d) has a

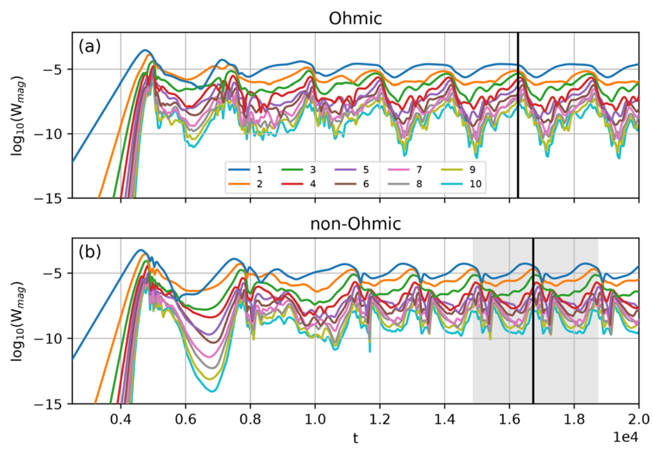

FIG. 2. Logarithms of magnetic fluctuation energies $W_{\rm mag}$ vs time t for toroidal modes n shown in different colors. (a) Ohmic sawtoothing case: black vertical line is at $t = 16\,264.959$, the time point shown in Fig. 4(a). (b) Non-Ohmic sawtoothing case: black vertical line is at $t = 16\,735.391$, the time point shown in Figs. 3, 4(b), and 8(a); shaded area has $14\,865 \leq t \leq 18\,745$, the time window shown in Fig. 5.

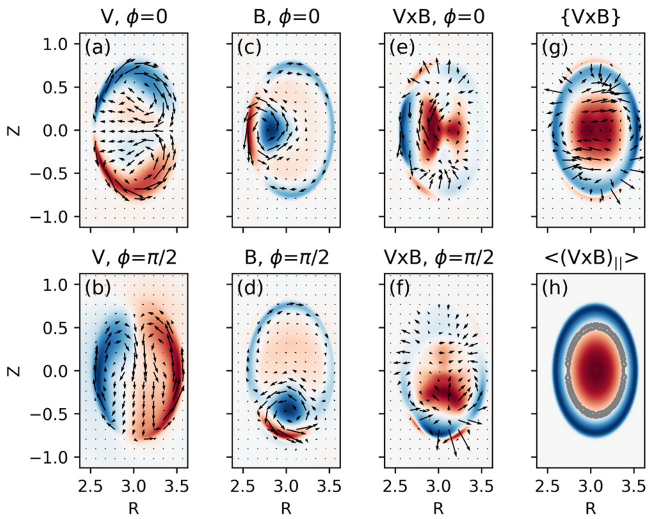

FIG. 3. Structures of velocity and magnetic field fluctuations in poloidal cross section leading to the dynamo EMF for the non-Ohmic sawtoothing case at the time point indicated by the black vertical line in Fig. 2(b). The major radius is R, and the vertical position is Z. (a) and (b) Velocity fluctuation $\tilde{\boldsymbol{V}}$ at toroidal phase angle ϕ of 0 and $\pi/2$, respectively. (c) and (d) Magnetic field fluctuation $\tilde{\boldsymbol{B}}$ at ϕ of 0 and $\pi/2$. (e) and (f) $\tilde{\boldsymbol{V}} \times \tilde{\boldsymbol{B}}$ at ϕ of 0 and $\pi/2$. (g) Toroidal average $\{\tilde{\boldsymbol{V}} \times \tilde{\boldsymbol{B}}\}$. (h) Parallel flux-surface average $\langle(\tilde{\boldsymbol{V}} \times \tilde{\boldsymbol{B}})_{\parallel}\rangle$, i.e., the dynamo EMF, where the $q = 1$ surface region is shown in gray between the red and blue regions. In all panels, blue represents positive and red negative numerical values, with darker color values for larger numerical magnitudes. For vector fields in (a) through (g), color refers to the toroidal component and arrows to components in the poloidal plane. Numerical scales vary in each panel.

helically localized tearing-like pattern. Their cross product $\tilde{\boldsymbol{V}} \times \tilde{\boldsymbol{B}}$ in Figs. 3(e) and 3(f) has a complicated helical shape, with a toroidal average $\{\tilde{\boldsymbol{V}} \times \tilde{\boldsymbol{B}}\}$ in Fig. 3(g) that is much more poloidally symmetric. Figure 3(h) shows the poloidal flux-surface average of the component of $\{\tilde{\boldsymbol{V}} \times \tilde{\boldsymbol{B}}\}$ parallel to the $n = 0$ $\{\boldsymbol{B}\}$ field, which is the dynamo EMF $\langle(\tilde{\boldsymbol{V}} \times \tilde{\boldsymbol{B}})_{\parallel}\rangle$ appearing as the last term on the left side of Eq. (1). The dynamo EMF is acting as negative or anti-current drive against the $n = 0$ current density in the region between the magnetic axis and the $q = 1$ surface and as positive current drive outside of the $q = 1$ surface, flattening the q profile.

The key features of the mean-field parallel Ohm's law balance are markedly similar in the Ohmic and non-Ohmic sawtoothing cases, as shown in Fig. 4. The Ohm's law (1) is rewritten in terms of the quantities derived from the NIMROD output data as

$$\langle E_{\mathrm{vac}\parallel}\rangle - \langle\partial_t A_{\parallel}\rangle + \langle(\tilde{\boldsymbol{V}} \times \tilde{\boldsymbol{B}})_{\parallel}\rangle = \langle\eta J_{\parallel}\rangle, \tag{2}$$

and these quantities are plotted in Fig. 4 for the respective times indicated by the black vertical lines in Fig. 2 vs major radius R at midplane, i.e., at vertical position $Z = 0$. Using the NIMROD data, we calculate the $n = 0$ electric field $\boldsymbol{E}$ as composed of two parts: the applied vacuum toroidal electric field present in the Ohmic case in Fig. 4(a) (purple), with magnitude $E_{\mathrm{vac}}(R) = V_{\mathrm{loop}}/R$, where V_{loop} is the feedback-controlled value, and $-\partial_t \boldsymbol{A}$ (blue), where $\boldsymbol{A}$ is the vector potential derived from the time-advanced $n = 0$ magnetic field $\boldsymbol{B}$, corresponding to the inductive $n = 0$ dynamics in either the Ohmic or non-Ohmic cases. The potential $\boldsymbol{A}(R, Z)$ has toroidal

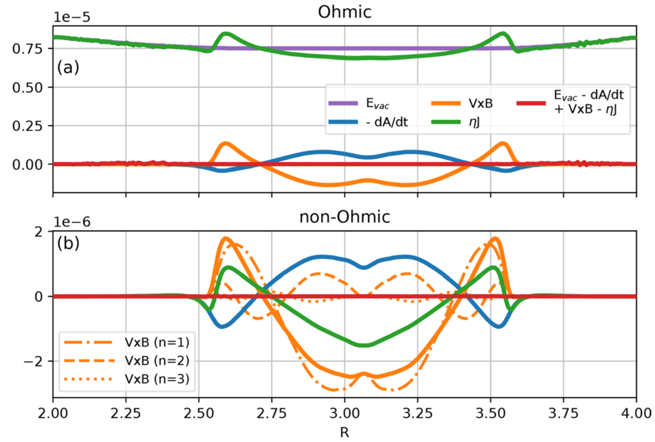

FIG. 4. Parallel flux-surface-average Ohm's law quantities as in Eq. (2) vs major radius R at midplane for the sawtoothing cases at the respective time points indicated by the black vertical lines in Fig. 2. The inductive $-\langle\partial_t A_{\parallel}\rangle$ is shown in blue, the dynamo EMF $\langle(\tilde{\boldsymbol{V}} \times \tilde{\boldsymbol{B}})_{\parallel}\rangle$ is in orange, the $\langle\eta J_{\parallel}\rangle$ curve is in green, and the Ohm's law residual, i.e., the difference of left and right sides of Eq. (2), is in red. (a) Ohmic case with the vacuum electric field $\langle E_{\mathrm{vac}\parallel}\rangle$ is shown in purple. The $\langle\eta J_{\parallel}\rangle$ curve shows a small amount of noise in the edge regions thought to be due to the flux-surface-averaging algorithm. (b) Non-Ohmic case for which the $\langle\eta J_{\parallel}\rangle$ curve represents only the time-varying part of the $n = 0$ current density J. Dash-dotted, dashed, and dotted orange curves are the $n = 1$, $n = 2$, and $n = 3$ components of the dynamo EMF, respectively.

component $\psi(R, Z)/R$, where $\psi(R, Z)$ is the poloidal magnetic flux per radian, and, given a toroidally symmetric $\boldsymbol{B} = \nabla \times \boldsymbol{A}$, a poloidal component given by elliptic integral expressions from Ref. 76 integrated over the toroidal magnetic field $B_{\phi}(R, Z)$ after the proper substitutions,

$$A_R(R, Z) = \int \frac{(Z - Z')}{2\pi R}\left(\frac{m}{4RR'}\right)^{1/2} B_{\phi}(R', Z') \times \left[\frac{2 - m}{2 - 2m}E(m) - K(m)\right]\mathrm{d}R'\mathrm{d}Z',$$

$$A_Z(R, Z) = \int \frac{1}{2\pi}\left(\frac{m}{4RR'}\right)^{1/2} B_{\phi}(R', Z') \times \left[\frac{mR' - (2 - m)R}{(2 - 2m)R}E(m) + K(m)\right]\mathrm{d}R'\mathrm{d}Z',$$

where the argument of the elliptic integrals $E(m)$ and $K(m)$ is $m = 4RR'/[(Z - Z')^2 + (R + R')^2]$. As the result satisfies $\nabla \cdot \boldsymbol{A} = 0$, this can be categorized as a Coulomb gauge calculation. The dynamo EMF term $\langle(\tilde{\boldsymbol{V}} \times \tilde{\boldsymbol{B}})_{\parallel}\rangle$ is plotted in orange. For the Ohmic case in Fig. 4(a), the $\langle\eta J_{\parallel}\rangle$ term (green) reflects the hollow η profile and peaked $n = 0$ J profile. In the non-Ohmic case in Fig. 4(b), however, the initial equilibrium J profile is not time-advanced, and the $\langle\eta J_{\parallel}\rangle$ represents only the smaller time-varying $n = 0$ component of J. To show that this analysis balances the simulated Ohm's law in either the Ohmic or non-Ohmic case, the Ohm's law residual, i.e., the difference of left and right sides of Eq. (2), is also shown in Figs. 4(a) and 4(b) (red).

As seen in Fig. 4(a) for the Ohmic sawtoothing case, $\langle\eta J_{\parallel}\rangle$ [right side of Eq. (2)] is mostly balanced by $\langle E_{\mathrm{vac}\parallel}\rangle$ [left side of Eq. (2)], and this pairing, only present for the Ohmic case, exhibits the key algorithmic difference between Ohmic and non-Ohmic cases. In both cases, the smaller inductive $-\langle \partial_t A_\parallel \rangle$ and dynamo EMF $\langle (\tilde{\boldsymbol{V}} \times \tilde{\boldsymbol{B}})_\parallel \rangle$ terms evidently balance the remainder of $\langle \eta J_\parallel \rangle$ in the core. We note that the dynamo EMF opposes the inductive $n = 0$ response $-\langle \partial_t A_\parallel \rangle$ at the times represented in both cases. We also observe in both cases that the dynamo EMF is dominated by its $n = 1$ component, as shown in Fig. 4(b) for the non-Ohmic case along with the smaller $n = 2$ and $n = 3$ components, with higher n components even smaller. We have not calculated poloidal mode numbers m for these data, but we do note that, as might be expected for fluctuations associated with a $q = m/n = 1$ resonance, the $n = 1$ has finite amplitude on the magnetic axis, while the higher-n components do not, which suggests $m = n$, in that $m > 1$ components would vanish on the axis.

To show the full Ohm's law dynamics and demonstrate how the fluctuation-induced dynamo EMF modulates the $n = 0$ profile in the sawtooth cycle, we show two full sawtooth cycles in time for the non-Ohmic case in Fig. 5, corresponding to the time window indicated in Fig. 2(b). Dynamics closely matching these are also present in the Ohmic case, which is not shown here for brevity. In Figs. 5(a) and 5(b), the magnetic W_{mag} and kinetic W_{kin} fluctuation energies are plotted. As seen earlier for W_{mag} and shown here for both W_{mag} and W_{kin}, these are dominated by $n = 1$ and to a lesser degree by $n = 2$. The W_{mag} waveforms, especially for the dominant n, are more complex than the W_{kin}, e.g., in the temporal nonmonotonicity of W_{mag} around the crash time for $n = 1$ and $n = 2$, and they tend to become more complex for higher n. The remaining panels of Fig. 5 show flux-surface quantities on the midplane. The core $n = 0$ q profile is shown in Fig. 5(c), evidencing Kadomtsev-style sawteeth as it oscillates about 1 with an amplitude on axis of roughly 0.05 (*i.e.*, $\Delta q_0 \approx 0.1$ at the crash). This activity is driven by the dynamo EMF $\langle (\tilde{\boldsymbol{V}} \times \tilde{\boldsymbol{B}})_\parallel \rangle$ shown in Fig. 5(d) as modulated by the inductive response $-\langle \partial_t A_\parallel \rangle$ shown in Fig. 5(e). Starting at around $t \approx 1.6\mathrm{E}4$, with $q_0 \approx 0.95$, as W_{mag} and W_{kin} grow, $\langle (\tilde{\boldsymbol{V}} \times \tilde{\boldsymbol{B}})_\parallel \rangle$ does as well, growing more negative on axis and more positive near the $q = 1$ surface, tending to flatten the current profile and drive q back above 1, which is the sawtooth crash. Note the black vertical lines indicating this crash time at the time point shown in Figs. 3, 4(b), and 8(a). During the crash, the inductive response opposes the dynamo EMF, as it qualitatively tends to do throughout the sawtooth cycle, highlighting the fundamental character of this dynamical feature. We observe that the minor radial boundary between positive and negative dynamo EMF propagates outward with time during the crash. After the crash, the q profile returns below 1, though that is also opposed by the $-\langle \partial_t A_\parallel \rangle$ inductive response, as the fluctuation energy is dissipating and the total $n = 0$ profile approaches its $t = 0$ condition. Note that during this sawtooth activity in this non-Ohmic case, the time-varying $\langle \eta J_\parallel \rangle$ term shown in Fig. 5(f) is consistently negative on axis, as the fluctuation-regulated MHD prevents the $n = 0$ current profile from again reaching its more peaked $t = 0$ state.

B. Steady state

The previous development shows how the spatiotemporal interplay between the fluctuation-induced dynamo EMF and the plasma's inductive response strongly influences the sawtooth cycle dynamics. In contrast, by increasing the plasma dissipation relative to that of the non-Ohmic sawtoothing case, in particular, the viscosity ν, thereby increasing the magnetic Prandtl number $P_{\mathrm{m}} \propto \nu/\eta$ and decreasing the Hartmann number $H \propto 1/\sqrt{\eta\nu}$, we simulate a tokamak that evolves into a steady state whose helical core nonetheless generates a dynamo EMF and resulting effect on the $n = 0$ current profile which we find to be similar to that for the sawtoothing case. The parameters for the case presented in this section are $P_{\mathrm{m}} = 10^3$ and $H \approx 3 \times 10^3$.

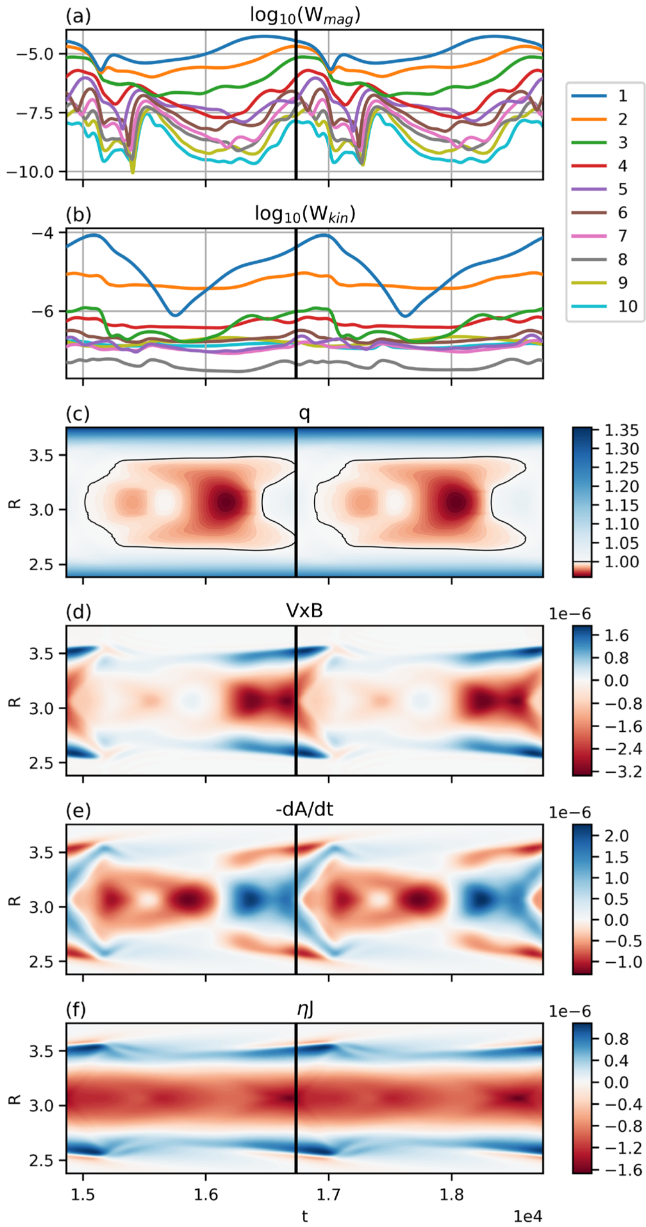

FIG. 5. Two sawtooth cycles vs time t for the non-Ohmic case in the time window indicated in Fig. 2(b). Logarithms of fluctuation energies for toroidal mode numbers n are shown in different colors, and the contour maps show flux-surface quantities vs R at midplane, zoomed in to show detail. Black vertical line is at $t = 16\,735.391$, the time point shown in Figs. 3, 4(b), and 8(a). (a) Magnetic fluctuation energies. (b) Kinetic fluctuation energies. (c) Safety factor q, with $q = 1$ shown as a black contour. (d) Dynamo EMF $\langle (\tilde{\boldsymbol{V}} \times \tilde{\boldsymbol{B}})_\parallel \rangle$. (e) Inductive electric field $-\langle \partial_t A_\parallel \rangle$. (f) The time-varying part of $\langle \eta J_\parallel \rangle$.

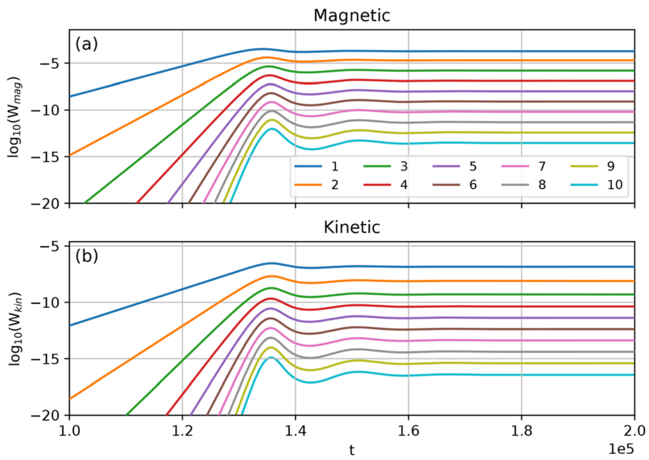

FIG. 6. Logarithms of fluctuation energies vs time t for toroidal modes n shown in different colors for increased-dissipation case ($P_m = 10^3$, $H \approx 3 \times 10^3$). (a) Magnetic fluctuation energies W_{mag}. (b) Kinetic fluctuation energies W_{kin}.

The magnetic and kinetic fluctuation energies for the increased-dissipation case are shown in Fig. 6. Here, unlike the sawtoothing cases, after the initial linear growth stage, temporal oscillations in fluctuation amplitudes are damped by the increased viscosity and become static in time, resulting in a steady state with a finite $n \geq 1$ helical distortion.

The helical distortion produces a steady $n = 0$ dynamo EMF that alone balances the resistive term in the parallel flux-surface-average Ohm's law, as shown in Fig. 7(a), a plot of the terms in Eq. (2) on midplane vs R. Comparing to Fig. 4(b) for the non-Ohmic sawtoothing case, here, the (blue) inductive term $-\langle \partial_t A_\parallel \rangle$ has vanished in this steady state, and the (orange) dynamo EMF $\langle (\tilde{\boldsymbol{V}} \times \tilde{\boldsymbol{B}})_\parallel \rangle$ arising from the steady helical distortion is solely responsible for driving the equilibrium $n = 0$ current profile distortion reflected in the resistive term $\langle \eta J_\parallel \rangle$ (green). This steady dynamo EMF has the same basic spatial profile and a similar magnitude to that in the sawtoothing case.

Figure 7(b) shows the corresponding $n = 0$ safety factor q profile (blue) on midplane vs R compared to the initial equilibrium profile (orange). Thus, the steady-state dynamo EMF does push the core q profile toward unity from below as it does in the sawtoothing case, but here, the increased dissipation suppresses its effect in comparison, such that the core q remains below unity.

The on-axis value of the static safety factor in Fig. 7(b) for this $H \approx 3 \times 10^3$ case is about $q_0 = 0.94$. We also performed simulations with higher H values (i.e., lower dissipation), estimating an upper limit on the H value clearly resulting in a steady helical core of about $H \gtrsim 7.5 \times 10^3$, for which $q_0 = 0.98$. At $H = 10^4$, the simulated tokamak fluctuation energies strongly oscillate at first and then damp slowly, and determining whether they would eventually achieve a steady state would require more simulation time than completed to date. At $H \approx 3 \times 10^4$, we again observe sawtoothing as in the cases above, which have $H = 10^5$.

As indicated earlier, the spatial structures of the dynamo EMF are similar in the sawtoothing and steady-state cases, which is exhibited in more detail in the Poincaré plots in Fig. 8. These show the projections of the respective helical distortions in terms of magnetic field line puncture points on poloidal planes, and in each case, there is a clear poloidal mode number $m = 1$ structure composed of a pair of helical magnetic axes. The key qualitative difference appears to be the overall smoother spatial format of the steady-state structure in Fig. 8(b) compared to the sawtoothing case in Fig. 8(a), perhaps due to the increased-dissipation parameter. This aspect of these $q \approx 1$ structures also appears to be reflected in the toroidal mode spectral width, which is more narrowly peaked at $n = 1$ in the steady-state case (as in Fig. 6) than in the sawtoothing case at the crash time [indicated by the black vertical line in Figs. 2(b) or 5(a)]. Note that the toroidal phase $\phi = 0$ for the magnetic field shown in both cases matches that in Fig. 3 for the sawtoothing case. Both of these results recall the "$m = 1$

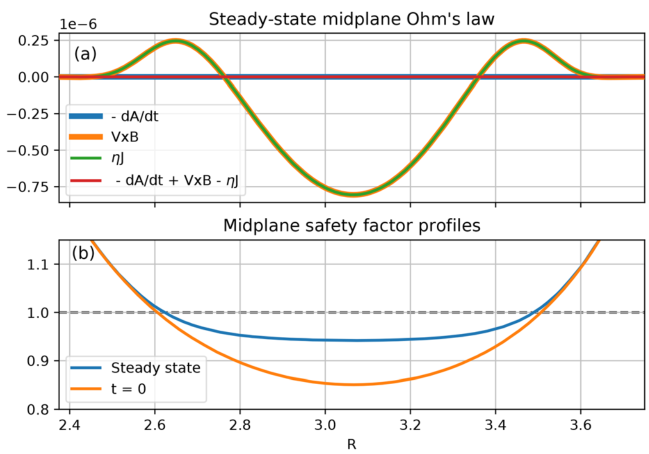

FIG. 7. Profiles vs major radius R at midplane for increased-dissipation case. (a) Steady-state parallel flux-surface-average Ohm's law quantities as in Eq. (2). The inductive $-\langle \partial_t A_\parallel \rangle$ is in blue, the dynamo EMF $\langle (\tilde{\boldsymbol{V}} \times \tilde{\boldsymbol{B}})_\parallel \rangle$ is in orange, the $\langle \eta J_\parallel \rangle$ curve is in green, and the Ohm's law residual is in red. Note that the dynamo EMF and the $\langle \eta J_\parallel \rangle$ curve overlap. (b) Initial ($t = 0$) equilibrium q profile in orange and steady-state profile in blue. Dashed line indicates $q = 1$.

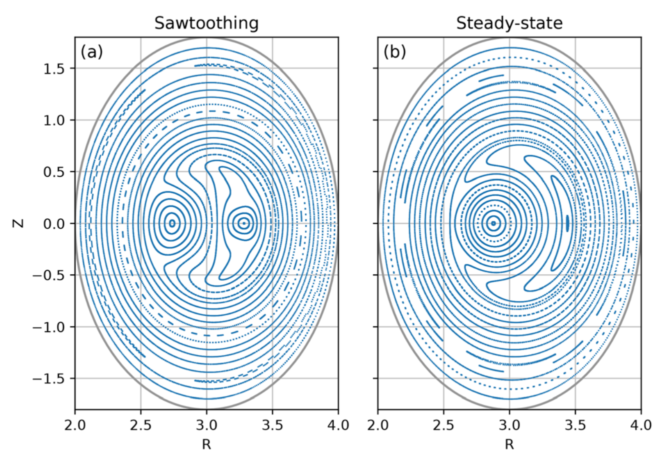

FIG. 8. Poincaré plots showing magnetic structure at toroidal phase $\phi = 0$ for (a) the non-Ohmic sawtoothing case at the time point indicated by the black vertical line in Figs. 2(b) or 5(a) and for (b) the increased-dissipation case in its steady state. The major radius is R, and the vertical position is Z.

convection cell" structure identified in early MHD simulations of tokamak sawteeth.[37]

IV. DISCUSSION

In summary, via NIMROD simulations of tokamak plasmas, we have shown how the $\langle(\tilde{\boldsymbol{V}} \times \tilde{\boldsymbol{B}})_{\|}\rangle$ dynamo EMF arises from the nonlinear interactions of fluctuations in a relatively simple zero-thermal-pressure, visco-resistive MHD model and modulates the $n = 0$ profile in a Kadomtsev-like sawtooth cycle. The basic dynamics and form of the dynamo effect are the same regardless of whether the simulation has an explicitly applied external loop voltage. We have shown the helical structure of the fluctuations leading to the EMF, that its composition is dominated by $n = 1$ fluctuations, and how its structure evolves radially as it drives the $n = 0$ evolution, flattening the current profile during the sawtooth crash, in tandem with the plasma's inductive response, which typically evolves in opposition to the dynamo. This coupling between dynamo EMF and inductive response, also observed previously in simulations of RFPs,[55] appears to be a key dynamical feature of tokamak sawteeth. Using otherwise identical tokamak simulation cases with increased scalar viscosity, i.e., decreased Hartmann number, we also show steady-state dynamo EMF structures produced by the resulting quiescent helical cores, finding them to be similar to the sawtooth cases at the crash. Thus, we can distinguish two fundamental properties of the core dynamo EMF in tokamak MHD: (1) its interaction with the plasma's inductive response in driving the sawtooth cycle and (2) its effect on the equilibrium profiles with or without a sawtooth cycle.

This work expands the description of the dynamo's central importance beyond its role in sawtoothing or sawtooth-free tokamak states with relatively quiescent core q profiles in finite-thermal-pressure MHD[28,33,35,69,70] to a detailed examination of its role in the continuous modulation of the q profile during the sawtooth cycle in zero-thermal-pressure MHD. As a corollary, in tandem with some other works in the context of specific tokamak phenomena,[64,65] the present analysis points to consideration of the dynamo effect in analyzing any MHD fluctuation activity correlated with current profile modification.

As future work, we foresee connections between MHD simulations like ours with experimental efforts (e.g., Ref. 72) to uncover the structure and evolution of fluctuation-induced EMF effects and, in particular, how they may interact with other key tokamak phenomena including tearing-mode triggering and transport.[8–14] We have noted earlier the apparent complexity of the magnetic fluctuation energies in our simulations, reminiscent of the compound character of sawteeth observed in other recent MHD simulations,[42] and further investigation of similar cases might elucidate this as well as possible wider effects. The simulations we presented involve a relatively simple MHD model compared to other recent efforts, and it would be interesting to examine how the addition of thermal pressure, two-fluid effects, and higher Lundquist number contribute to the fundamental aspects of the dynamo EMF described here.

ACKNOWLEDGMENTS

This material is based upon work supported by the U.S. Department of Energy, Office of Science, Office of Fusion Energy Sciences, under Award No. DE-SC0019003. The authors thank Carl Sovinec for helpful discussions related to this work.

AUTHOR DECLARATIONS

Conflict of Interest

The authors have no conflicts to disclose.

Author Contributions

K. J. McCollam: Conceptualization (equal); Data curation (lead); Formal analysis (lead); Funding acquisition (supporting); Investigation (lead); Methodology (lead); Project administration (supporting); Resources (equal); Software (lead); Visualization (lead); Writing – original draft (lead); Writing – review & editing (equal). **B. E. Chapman:** Conceptualization (equal); Funding acquisition (lead); Methodology (supporting); Project administration (lead); Resources (equal); Supervision (lead); Writing – review & editing (equal). **J. S. Sarff:** Conceptualization (equal); Funding acquisition (supporting); Methodology (supporting); Writing – review & editing (equal). **R. A. Myers:** Conceptualization (supporting); Methodology (supporting); Writing – review & editing (equal). **M. D. Pandya:** Conceptualization (supporting); Methodology (supporting); Writing – review & editing (equal). **R. Xie:** Conceptualization (supporting); Methodology (supporting); Writing – review & editing (equal).

DATA AVAILABILITY

The data that support the findings of this study are available from the corresponding author upon reasonable request.

REFERENCES

1S. von Goeler, W. Stodiek, and N. Sauthoff, Phys. Rev. Lett. **33**, 1201 (1974).
2R. J. Hastie, Astrophys. Space Sci. **256**, 177 (1997).
3R. Fischer, A. Bock, A. Burckhart, O. P. Ford, L. Giannone, V. Igochine, M. Weiland, M. Willensdorfer, and the ASDEX Upgrade Team, Nucl. Fusion **59**, 056010 (2019).
4O. Samoylov, V. Igochine, A. Stegmeir, and H. Zohm, J. Plasma Phys. **88**, 905880116 (2022).
5V. Igochine, Phys. Plasmas **30**, 120502 (2023).
6T. C. Hender, J. Wesley, J. Bialek, A. Bondeson, A. H. Boozer, R. J. Buttery, A. Garofalo, T. Goodman, R. S. Granetz, Y. Gribov, O. Gruber, M. Gryaznevich, G. Giruzzi, S. G. nter, N. Hayashi, P. Helander, C. C. Hegna, D. F. Howell, D. A. Humphreys, G. T. A. Huysmans, A. W. Hyatt, A. Isayama, S. C. Jardin, Y. Kawano, A. Kellman, C. Kessel, H. R. Koslowski, R. J. L. Haye, E. Lazzaro, Y. Q. Liu, V. Lukash, J. Manickam, S. Medvedev, V. Mertens, S. V. Mirnov, Y. Nakamura, G. Navratil, M. Okabayashi, T. Ozeki, R. Paccagnella, G. Pautasso, F. Porcelli, V. D. Pustovitov, V. Riccardo, M. Sato, O. Sauter, M. J. Schaffer, M. Shimada, P. Sonato, E. J. Strait, M. Sugihara, M. Takechi, A. D. Turnbull, E. Westerhof, D. G. Whyte, R. Yoshino, H. Zohm, and the ITPA MHD, Disruption and Magnetic Control Topical Group, Nucl. Fusion **47**, S128 (2007).
7P. Rodriguez-Fernandez, N. T. Howard, M. J. Greenwald, A. J. Creely, J. W. Hughes, J. C. Wright, C. Holland, Y. Lin, and F. Sciortino, J. Plasma Phys. **86**, 865860503 (2020).
8M. F. F. Nave, J. Rapp, T. Bolzonella, R. Dux, M. J. Mantsinen, R. Budny, P. Dumortier, M. von Hellermann, S. Jachmich, H. R. Koslowski, G. Maddison, A. Messiaen, P. Monier-Garbet, J. Ongena, M. E. Puiatti, J. Strachan, G. Telesca, B. Unterberg, M. Valisa, P. de Vries, and contributors to the JET-EFDA Workprogramme, Nucl. Fusion **43**, 1204 (2003).
9D. P. Brennan, S. E. Kruger, T. A. Gianakon, and D. D. Schnack, Nucl. Fusion **45**, 1178 (2005).
10B. Geiger, M. Garcia-Munoz, R. Dux, F. Ryter, G. Tardini, L. B. Orte, I. G. J. Classen, E. Fable, R. Fischer, V. Igochine, R. M. McDermott, and the ASDEX Upgrade Team, Nucl. Fusion **54**, 022005 (2014).
11L. Bardóczi, N. C. Logan, and E. J. Strait, Phys. Rev. Lett. **127**, 055002 (2021).

[12]A. Bierwage, K. Shinohara, Y. O. Kazakov, V. G. Kiptily, P. Lauber, M. Nocente, Ž. Štancar, S. Sumida, M. Yagi, J. Garcia, S. Ide, and JET Contributors, Nat. Commun. **13**, 3941 (2022).
[13]P. J. Bonofiglo, M. Podest, M. Vallar, N. N. Gorelenkov, V. Kiptily, R. B. White, C. Giroud, S. Brezinsek, and J. E. T. Contributors, Nucl. Fusion **62**, 112002 (2022).
[14]R. J. L. Haye, C. Chrystal, E. J. Strait, J. D. Callen, C. C. Hegna, E. C. Howell, M. Okabayashi, and R. S. Wilcox, Nucl. Fusion **62**, 056017 (2022).
[15]O. Sauter, E. Westerhof, M. L. Mayoral, B. Alper, P. A. Belo, R. J. Buttery, A. Gondhalekar, T. Hellsten, T. C. Hender, D. F. Howell, T. Johnson, P. Lamalle, M. J. Mantsinen, F. Milani, M. F. F. Nave, F. Nguyen, A. L. Pecquet, S. D. Pinches, S. Podda, and J. Rapp, Phys. Rev. Lett. **88**, 105001 (2002).
[16]I. T. Chapman, Plasma Phys. Controlled Fusion **53**, 013001 (2011).
[17]J. P. Graves, I. T. Chapman, S. Coda, M. Lennholm, M. Albergante, and M. Jucker, Nat. Commun. **3**, 624 (2012).
[18]E. Lerche, M. Lennholm, I. S. Carvalho, P. Jacquet, M. Mantsinen, P. Dumortier, D. V. Eester, J. P. Graves, P. Card, C. Noble, and JET Contributors, Nucl. Fusion **60**, 126037 (2020).
[19]R. J. Buttery, B. Covele, J. Ferron, A. Garofalo, C. T. Holcomb, T. Leonard, J. M. Park, T. Petrie, C. Petty, G. Staebler, E. J. Strait, and M. Van Zeeland, J. Fusion Energy **38**, 72 (2019).
[20]M. R. Wade, T. C. Luce, R. J. Jayakumar, P. A. Politzer, A. W. Hyatt, J. R. Ferron, C. M. Greenfield, M. Murakami, C. C. Petty, R. Prater, J. C. DeBoo, R. J. L. Haye, P. Gohil, and T. L. Rhodes, Nucl. Fusion **45**, 407 (2005).
[21]C. C. Petty, M. E. Austin, C. T. Holcomb, R. J. Jayakumar, R. J. La Haye, T. C. Luce, M. A. Makowski, P. A. Politzer, and M. R. Wade, Phys. Rev. Lett. **102**, 045005 (2009).
[22]T. C. Luce, C. D. Challis, S. Ide, E. Joffrin, Y. Kamada, P. A. Politzer, J. Schweinzer, A. C. C. Sips, J. Stober, G. Giruzzi, C. E. Kessel, M. Murakami, Y.-S. Na, J. M. Park, A. R. Polevoi, R. V. Budny, J. Citrin, J. Garcia, N. Hayashi, J. Hobirk, B. F. Hudson, F. Imbeaux, A. Isayama, D. C. McDonald, T. Nakano, N. Oyama, V. V. Parail, T. W. Petrie, C. C. Petty, T. Suzuki, M. R. Wade, and the ITPA Integrated Operation Scenario Topical Group Members, the ASDEX-Upgrade Team, the DIII-D Team, JET EFDA Contributors, and the JT-60U Team, Nucl. Fusion **54**, 013015 (2014).
[23]F. Turco, T. Petrie, T. Osborne, C. C. Petty, T. C. Luce, B. Grierson, T. Odstrcil, M. A. V. Zeeland, D. Liu, L. Casali, W. Boyes, S. P. Smith, H. Shen, M. Kostuk, and D. Brennan, Nucl. Fusion **63**, 036020 (2023).
[24]B. B. Kadomtsev, Sov. J. Plasma Phys. **1**, 389 (1975).
[25]J. A. Wesson, Plasma Phys. Controlled Fusion **28**, 243 (1986).
[26]A. J. Lichtenberg, K. Itoh, S.-I. Itoh, and A. Fukuyama, Nucl. Fusion **32**, 495 (1992).
[27]Y. I. Kolesnichenko, Y. V. Yakovenko, D. Anderson, M. Lisak, and F. Wising, Phys. Rev. Lett. **68**, 3881 (1992).
[28]S. C. Jardin, I. Krebs, and N. Ferraro, Phys. Plasmas **27**, 032509 (2020).
[29]M. T. Beidler, P. A. Cassak, S. C. Jardin, and N. M. Ferraro, Plasma Phys. Controlled Fusion **59**, 025007 (2017).
[30]Y. B. Nam, J. S. Ko, G. H. Choe, Y. Bae, M. J. Choi, W. Lee, G. S. Yun, S. Jardin, and H. K. Park, Nucl. Fusion **58**, 066009 (2018).
[31]W. W. Heidbrink and B. S. Victor, Phys. Plasmas **27**, 080701 (2020).
[32]D. Liu, W. Fox, S. Bose, H. Ji, S. Jardin, and N. Ferraro, Phys. Plasmas **31**, 032512 (2024).
[33]Q. Yu, S. G. nter, and K. Lackner, Nucl. Fusion **64**, 086053 (2024).
[34]A. Hussain, L. Xu, H. Quan, Y. Chao, H. Lian, T. Zhou, G. Li, and E. A. S. T. Team, Phys. Scr. **100**, 055608 (2025).
[35]H. Zhang, M. H. lzl, I. Krebs, A. Burckhart, A. Bock, S. Günter, V. Igochine, K. Lackner, R. Ramasamy, H. Zohm, and the JOREK Team, and the ASDEX Upgrade Team, Nucl. Fusion **65**, 066001 (2025).
[36]A. Sykes and J. A. Wesson, Phys. Rev. Lett. **37**, 140 (1976).
[37]R. E. Denton, J. F. Drake, and R. G. Kleva, Phys. Fluids **30**, 1448 (1987).
[38]J. A. Holmes, B. A. Carreras, L. A. Charlton, V. E. Lynch, R. J. Hastie, and T. C. Hender, Phys. Fluids **31**, 1202 (1988).
[39]A. Y. Aydemir, J. C. Wiley, and D. W. Ross, Phys. Fluids B: Plasma Phys. **1**, 774 (1989).
[40]F. D. Halpern, H. Lütjens, and J.-F. Luciani, Phys. Plasmas **18**, 102501 (2011).
[41]A. Y. Aydemir, J. Y. Kim, B. H. Park, and J. Seol, Phys. Plasmas **22**, 032304 (2015).
[42]J.-H. Ahn, X. Garbet, H. Lütjens, A. Marx, T. Nicolas, R. Sabot, J.-F. Luciani, R. Guirlet, O. Février, and P. Maget, Phys. Plasmas **23**, 052509 (2016).
[43]D. Bonfiglio, M. Veranda, S. Cappello, L. Chac n, and D. F. Escande, Plasma Phys. Controlled Fusion **59**, 014032 (2017).
[44]O. Février, T. Nicolas, P. Maget, J.-H. Ahn, X. Garbet, and H. Lütjens, Nucl. Fusion **58**, 096008 (2018).
[45]W. Shen and F. Porcelli, Nucl. Fusion **58**, 106035 (2018).
[46]M. Veranda, D. Bonfiglio, S. Cappello, G. di Giannatale, and D. F. Escande, Nucl. Fusion **60**, 016007 (2020).
[47]W. Zhang, Z. W. Ma, F. Porcelli, H. W. Zhang, and X. Wang, Nucl. Fusion **60**, 096013 (2020).
[48]C. B. Smiet, G. J. Kramer, and S. R. Hudson, Plasma Phys. Controlled Fusion **62**, 025007 (2020).
[49]S. Munaretto, B. E. Chapman, B. S. Cornille, A. M. DuBois, K. J. McCollam, C. R. Sovinec, A. F. Almagri, and J. A. Goetz, Nucl. Fusion **60**, 046024 (2020).
[50]B. S. Cornille, M. T. Beidler, S. Munaretto, B. E. Chapman, D. Del-Castillo-Negrete, N. C. Hurst, J. S. Sarff, and C. R. Sovinec, Phys. Plasmas **29**, 052510 (2022).
[51]D. D. Schnack, E. J. Caramana, and R. A. Nebel, Phys. Fluids **28**, 321 (1985).
[52]Y. L. Ho and G. G. Craddock, Phys. Fluids B: Plasma Phys. **3**, 721 (1991).
[53]D. J. Den Hartog, J. T. Chapman, D. Craig, G. Fiksel, P. W. Fontana, S. C. Prager, and J. S. Sarff, Phys. Plasmas **6**, 1813 (1999).
[54]S. Cappello, D. Bonfiglio, and D. F. Escande, Phys. Plasmas **13**, 056102 (2006).
[55]D. Bonfiglio, S. Cappello, and D. F. Escande, AIP Conf. Proc. **871**, 3 (2006).
[56]J. P. Sauppe and C. R. Sovinec, Phys. Plasmas **24**, 056107 (2017).
[57]P. Piovesan, D. Bonfiglio, M. Cianciosa, T. Luce, N. Taylor, D. Terranova, F. Turco, R. Wilcox, A. Wingen, S. Cappello, C. Chrystal, D. Escande, C. Holcomb, L. Marrelli, C. Paz-Soldan, L. Piron, I. Predebon, B. Zaniol, D.-D. The, and R.-M. Teams, Nucl. Fusion **57**, 076014 (2017).
[58]A. Al Karkhy, P. K. Browning, G. Cunningham, S. J. Gee, and M. G. Rusbridge, Phys. Rev. Lett. **70**, 1814 (1993).
[59]C. R. Sovinec, J. M. Finn, and D. del Castillo-Negrete, Phys. Plasmas **8**, 475 (2001).
[60]P. L. Garc a-Mart nez, L. G. Lampugnani, and R. Farengo, Phys. Plasmas **21**, 122511 (2014).
[61]X. Z. Tang and A. H. Boozer, Phys. Plasmas **11**, 2679 (2004).
[62]J. B. O'Bryan and C. R. Sovinec, Plasma Phys. Controlled Fusion **56**, 064005 (2014).
[63]F. Ebrahimi, Phys. Plasmas **23**, 120705 (2016).
[64]F. Ebrahimi, Phys. Plasmas **24**, 056119 (2017).
[65]C. R. Sovinec and K. J. Bunkers, Plasma Phys. Controlled Fusion **61**, 024003 (2019).
[66]W. Z. Mao, W. X. Ding, H. Q. Liu, A. Ti, D. L. Brower, H. Lian, Y. Q. Chu, L. Zeng, H. L. Zhao, L. Zhang, J. P. Qian, Q. Zang, X. Z. Gong, L. Q. Hu, L. Q. Xu, C. Zhou, T. Lan, A. D. Liu, J. L. Xie, G. Zhuang, Y. T. Song, B. N. Wan, and J. G. Li, Phys. Rev. Res. **5**, L022047 (2023).
[67]B. Li, J. P. Levesque, G. A. Navratil, and M. E. Mauel, Nucl. Fusion **64**, 046020 (2024).
[68]W. Boyes, F. Turco, J. Hanson, G. A. Navratil, A. Turnbull, A. Hyatt, T. Luce, W. Meyer, A. O. Nelson, T. Odstrcil, T. Osborne, F. Scotti, A. Welander, and A. Wingen, Nucl. Fusion **64**, 124005 (2024).
[69]S. C. Jardin, N. Ferraro, and I. Krebs, Phys. Rev. Lett. **115**, 215001 (2015).
[70]I. Krebs, S. C. Jardin, S. Günter, K. Lackner, M. Hoelzl, E. Strumberger, and N. Ferraro, Phys. Plasmas **24**, 102511 (2017).
[71]J. L. Luxon, Nucl. Fusion **42**, 614 (2002).
[72]T. E. Benedett, J. Chen, D. L. Brower, and W. X. Ding, Plasma Phys. Controlled Fusion **66**, 085009 (2024).
[73]C. R. Sovinec, A. H. Glasser, T. A. Gianakon, D. C. Barnes, R. A. Nebel, S. E. Kruger, D. D. Schnack, S. J. Plimpton, A. Tarditi, and M. S. Chu, J. Comput. Phys. **195**, 355 (2004).
[74]E. C. Howell and C. R. Sovinec, Comput. Phys. Commun. **185**, 1415 (2014).
[75]S. Cappello and D. F. Escande, Phys. Rev. Lett. **85**, 3838 (2000).
[76]R. H. Good, Eur. J. Phys. **22**, 119 (2001).